Hindawi
Adsorption Science & Technology
Volume 2022, Article ID 7693472, 12 pages
https://doi.org/10.1155/2022/7693472

Research Article

Poly-3-Methyl Aniline-Assisted Spherical PbS Quantum Dots through the Ionic Adsorption Deposition Method as a Novel and Highly Efficient Photodetector in UV, Vis, and NIR Regions

N. M. A. Hadia,[1,2] Sayeda Eid,[3] Mohamed Shaban,[3,4] S. H. Mohamed,[5] Asmaa M. Elsayed,[3,6] Ashour M. Ahmed,[3] Meshal Alzaid,[1] Ahmed Adel A. Abdelazeez,[7] Wassim El Malti,[8] and Mohamed Rabia[3,9]

[1]*Physics Department, College of Science, Jouf University, Al-Jouf, Sakaka, P.O. Box 2014, Saudi Arabia*
[2]*Basic Sciences Research Unit, Jouf University, Al-Jouf, Sakaka, P.O. Box 2014, Saudi Arabia*
[3]*Nanophotonics and Applications Lab, Physics Department, Faculty of Science, Beni-Suef University, Beni-Suef 62514, Egypt*
[4]*Department of Physics, Faculty of Science, Islamic University of Madinah, Prince Naifbin Abdulaziz, Al Jamiah, Madinah 42351, Saudi Arabia*
[5]*Physics Department, Faculty of Science, Sohag University, 82524 Sohag, Egypt*
[6]*TH-PPM Group, Physics Department, Faculty of Science, Beni-Suef University, Beni-Suef 62514, Egypt*
[7]*Nanoscale Science, Chemistry Department, University of North Carolina at Charlotte, Charlotte, North Carolina, USA*
[8]*College of Engineering and Technology, American University of the Middle East, Kuwait*
[9]*Nanomaterials Science Research Laboratory, Chemistry Department, Faculty of Science, Beni-Suef University, Beni-Suef 62514, Egypt*

Correspondence should be addressed to Wassim El Malti; wassim.elmalti@aum.edu.kw
and Mohamed Rabia; mohamedchem@science.bsu.edu.eg

Received 1 May 2022; Revised 23 June 2022; Accepted 7 July 2022; Published 30 July 2022

Academic Editor: Mohammad Saad Algamdi

This study describes the preparation and characterization of glass/poly-3-methyl aniline (P3MA)/PbS quantum dot (QD) optoelectronic photodetector to detect and sense the light in broad spectral regions of UV, Vis, and NIR. This work is carried out to solve the drawbacks of other studs that prepare detectors in just one or two optical regions. Previous studies have used high-priced techniques. The deposition of P3MA on the glass surface was carried out by in situ oxidation process. Then, this polymer film was used to assist the deposition of PbS-QD particles through the ionic adsorption deposition method. The latter was performed using four different concentrations of $Pb(NO_3)_2$ solution (0.01, 0.03, 0.05, and 0.07 M) to form four P3MA/PbS composites: I, II, III, and IV, respectively. The chemical structure, morphologies, and electrical and optical properties of these composites were determined using different analytical tools. The SEM confirmed the formation of spherical QD particles of PbS on the P3MA surface. The TEM analysis showed that the composite has an average size of 5 nm, with the interatomic distances of 0.4 nm. Furthermore, the optical band gap values were 1.53, 1.52, 1.50, and 1.51 eV, respectively. The optoelectronic device could detect and sense light from 390 to 636 nm under various optical wavelengths. The produced current density (J_{ph}) values decreased from 0.029 mA.cm^{-2} at 390 nm to 0.022 mA.cm^{-2} at 500 nm and then increased until 0.024 mA.cm^{-2} at 636 nm. The light sensing was determined through the photoresponsivity (R) and detectivity (D) parameters, in which the photodetector has R and D values of 0.29 mA.cm^{-2} and 6.5×10^7 Jones, respectively. Finally, a simple mechanism was proposed to explain the light sensing through the prepared optoelectronic device. Soon, our team works on the industrial applications of this optoelectronic device in the industry field related to the great optoelectronic device technical properties and its low cost and easy preparation.

1. Introduction

Light is an essential energy source in our life, from which humans, animals, and plants obtain their warmth and vision. All the natural or artificial photosynthesis reactions are carried out depending on the light.

The development of optoelectronic devices has become an important demand for the current technology devices. The optoelectronic devices are applied in many essential fields such as cameras, street lighting, solar devices, spacecraft, army laser devices, and smart windows [1–3]. The main idea of the photodetector is that it works by photodetection under different intensities or wavelengths. The photons activate the photodetector surface, liberating a hot electron that can polarize the surface. Then, the current density (J_{ph}) values are produced [4, 5]. These values are directly proportional to the light intensity in most semiconductor materials, i.e., more photon flux and more electrons liberated and collected on the surface. J_{ph} values represent the rate of the liberated electrons and give the resonance motion. The photodetector material sensitivity to light is expressed in the photoresponsivity (R) and detectivity (D) to light flux that increases with these J_{ph} values. J_{ph} is the main function of laws related to both R and D [4].

Metal oxide, sulfide, and nitrides are all examples of materials used as photodetectors [1, 4, 6–9]. These materials detect light via the acceptance of the photon flux through their active sites. Therefore, all the researchers are interested in increasing the active sites on these materials by increasing the surface area. This process can be done by synthesizing and fabricating them with specific geometric shapes such as nanorods, nanowires, nanotubes, and nanosheets [10–12].

Previous studies on light detection and sensing using inorganic oxide materials were reported in the literature. Wang et al. [11] worked on CuO nanowires, as a high surface area nanomaterial, for light detection in the IR region. Their study produced a small J_{ph} value (20 μA) at a high applied bias voltage of +5 V.

Bai and Zhang [12] incorporated ZnO in CuO, in which there were few enhancements in the produced J_{ph} values of 107 μA at +1 V. Also, Hong et al. [13] prepared a photodetector including heterojunctions based on Si materials, and they applied a bias of 0 V. The produced J_{ph} increased to 4.5 μA. Shuai et al. have prepared CdS-ZnO composite as an optoelectronic material; the produced J_{ph} value and responsivity were very small [14]. By the same manner, there were some studies carried out on TiO2 for light detection, and the efficiency value has not reached 1% [15].

Recently, many scientific works described the replacement of oxides, sulfides, and nitrides with polymer materials [16, 17]. This is related to the high advantages of these materials in the optoelectronic field represented in the increased stability and composite contacts and their excellent sensitivity [18, 19]. Nevertheless, they possess economic advantages such as low cost, mass production, and easy preparation. The effect of light on the polymer motivates the electron-hole pair generation, in which the generated electrons oscillate on the chain surface for J_{ph} production.

Many studies were conducted using polymers as an optoelectronic material. Poly-3-hexylthiophene materials were applied as a photodetector for light sensing inside the eye-retina with acceptable light response [20]. In other studies polymethyl methacrylate (PMMA)/styrene/carbon nanotube [14], Fe-doped PMMA [21], and polyvinylpyrrolidone/$CsPbBr_3$ composite were implemented. However, the J_{ph} was very low, 0.01 mA at 2 V [22]. Theoretical studies were performed by implementing aniline derivatives, such as benzodithiophene/fluorine. The resulting composites responded to light with enhanced optical properties [23]. In addition, experimental studies were carried out on triphenylamine, and the J_{ph} was 0.001 mA at 0 V [24].

Although the described studies worked on the polymer applications as an optoelectronic device, there are still some drawbacks. The produced J_{ph} is low, about 0.001 to 0.1 $mA.cm^{-2}$, with low responsivity. Moreover, some other studies showed low reproducibility and small responsivity values. Last but not least, the previously prepared polymer optoelectronic materials can work in just one region of UV, Vis, or IR.

The current study was carried out to overcome many drawbacks present in the previous studies. P3MA/PbS optoelectronic photodetector with high active surface sites was synthesized. The prepared photodetector can sense the light in UV, Vis, or NIR regions with good R and D values. The optoelectronic responded well to light under on/off chopped light with high reproducibility.

In this work, P3MA was deposited on glass substrates using the in situ polymerization process. Then, the glass/P3MA was used to assist in further deposition of spherical PbS-QD particles through the ionic adsorption deposition method. The analyses of P3MA/PbS composites were conducted using different analytical tools such as SEM, TEM, FTIR, and optical measurements. The electrochemical measurements were carried out through CHI660E PowerStation. The effect of light wavelengths from 390 to 636 nm and the reproducibility of on/off chopped current were examined. Finally, a plausible mechanism was proposed for light sensing using the prepared optoelectronic device.

2. Materials and Methods

2.1. Materials. P3MA and $(NH_4)_2S_2O_8$ were purchased from Rankem (India) and Winlab (UK) companies, respectively. Dimethyl sulfoxide (DMSO) was purchased from Sigma-Aldrich, USA. Acetic acid (CH_3COOH), lead (II) nitrate $Pb(NO_3)_2$, sodium sulfate (Na_2SO_4), iodine (I_2), and sodium iodide (KI) were purchased from El-Naser Company, Egypt.

2.2. Preparation of P3MA/PbS-QD Composites. P3MA was prepared through the in situ oxidation polymerization method on glass. 3-Methyl aniline (0.1 M) was dissolved in 0.5 M CH_3COOH under ultrasonic effect. Similarly, 0.15 M $(NH_4)_2S_2O_8$ (oxidant) was dissolved. Then, the latter was suddenly added over the 3-methyl aniline solution in the presence of glass. After 1 h, a complete precipitate was formed from P3MA over a glass, glass/P3MA, and dried at 60°C for 12 h.

P3MA/PbS-QD composites are synthesized through the surface adsorption process. The glass/P3MA is immersed in different concentrations of Pb^{2+} ions 0.01, 0.03, 0.05, and 0.07 M at 25°C for 2 h. Through this process, the adsorption of Pb^{2+} over the P3MA surface has occurred. Subsequently, the glass/P3MA/PbS composite films were dried and then immersed in (0.01 M) thiourea solution at 60°C for 15 min. The reaction between the P3MA and Pb^{2+} led to the formation of glass/P3MA/PbS-QD composites. According to the concentrations of Pb^{2+}, the composites were classified as composite I (0.01 M Pb^{2+}), composite II (0.03 M Pb^{2+}), composite III (0.05 M Pb^{2+}), and composite IV (0.07 M Pb^{2+}).

2.3. Characterization of the Prepared QD Composites. The crystal structures and surface morphology of P3MA and P3MA/PbS were investigated using X-ray diffraction (XRD) PANalytical Pro, Holland, and Transmission Electron Microscope, JEOL JEM-2100. Moreover, the structures were examined using Fourier transform infrared (FTIR) Shimadzu 340 Jasco spectrophotometer. The morphologies of the samples were determined using scanning electron microscopy (SEM) ZEISS, Gemini. The optical analysis was achieved using Shimadzu UV/Vis spectrophotometer.

2.4. Electrochemical Measurements. All the electrochemical measurements of the prepared optoelectronic photodetector were conducted on the electrochemical workstation (CHI660E) in the voltage range from -1 to +1 V (Figure 1). A xenon lamp (100 mW.cm^{-2}) was used as a source of the simulated light, in which glass/P3MA/PbS (composite III) represents the photoelectrode. Ag pastes were used as electrodes on the two sides of the photodetector. The effect of the light wavelength (390-636 nm) on the prepared photodetector performance and the on/off chopped light reproducibility were assessed. All the measurements were carried out at room temperature (25°C) and under atmospheric conditions.

3. Results and Discussion

3.1. Characterization of the Prepared QD/Nanostructures. The morphological analyses of P3MA, PbS, and P3MA/PbS-QD structured thin films are shown in Figure 2. P3MA (Figure 2(a)) has a nanopore network consisting of nanoparticle agglomerates. The inserted figure shows a highly homogenous and porous structure. This structure is the key of the composite formation, in which the additional materials can penetrate or lodge inside the frame and form a high compact nanocomposite. Likewise, Figure 2(b) shows that the PbS-QD particles have a spherical shape inside and outside the P3MA network with increasing white color. These spherical shapes increase with increasing the Pb^{2+} concentrations from 0.01 to 0.07 M, as shown in Figures 2(b)–2(e), respectively. Moreover, Figure 2(f) shows the SEM image of the porous PbS-QD particle agglomerate, forming a nanostructure. This behavior is matched well with the previous literature [25–27].

ImageJ software was used to determine the cross-section and morphology with high clarity to confirm the morphological structures of the prepared materials. Figure 3(a) shows the high porosity of the P3MA network, which acts as the site to receive the PbS-QD particles as seen in Figures 3(b)–3(e) with the different Pb^{2+} concentrations. The spherical white shapes increase with increasing the Pb^{2+} concentrations and accumulate on the surface and inside the porous network. Furthermore, Figure 3(f) shows the PbS cross-section and morphology, in which the porous structure appears clearly with QD particle agglomerates.

These morphological properties of the P3MA/PbS composite were expected to have a high-efficiency optical absorption behavior, solely collecting each QD particle's properties.

Based on the encouraging specifications seen in composite III, the TEM image of the latter is presented in Figures 4(a) and 4(b) using different magnifications. It shows that the composite was formed with high symmetry, and the PbS and P3MA are well embedded in each other. Figure 4(b) shows the actual particle sizes of the composite with an average size of 5 nm. Moreover, the interatomic distances for P3MA are about 0.4 nm. These morphological properties confirm the ability of the composite to be applied as an optoelectronic material with high optical absorption behavior related to the high P3MA and PbS-QD material junctions.

Subsequently, the phase structure and particle sizes of P3MA, PbS, and P3MA/PbS-QD composites I, II, III, and IV were confirmed using the XRD analyses as shown in Figure 4(c). The P3MA XRD structure (red curve) includes one peak at $2\theta = 25.55^{\circ}$ for the growth direction (200), confirming the semicrystalline nature of the P3MA [25]. On the other hand, the PbS XRD pattern (black line) comprises eight peaks at $2\theta = 25.98^{\circ}$, 30.17°, 43.12°, 51.14°, 53.70°, 62.54, 68.82°, and 71.01°, confirming the crystalline nature of the prepared PbS-QD particles. The peaks correspond to the growth planes (110), (111), (022), (132), (170), (222), (311), and (133), respectively. From Scherrer's formula [26], $D = 0.9\lambda/W \cos\theta$, the average crystal sizes of PbS are 6 to 5 nm depending on the full width at half maximum (W), X-ray wavelength, and Bragg's angle. The XRD patterns of P3MA/PbS composites I, II, III, and IV (Figure 4(c)) confirm their formation due to the presence of a new peak appearing at 64.5°. Moreover, slight shifts toward lower 2θ angles in the positions of the peaks compared to the P3MA and PbS-QD particles can be noticed. This is due to the interaction and interferences between the composite constituents [27]. In addition, the P3MA has a new peak at $2\theta = 33.6^{\circ}$, which corresponds to the growth direction (120) [25]. For the composite PbS, new peaks at $2\theta = 39.34$, 64.50, and 72.24° are also emerged and related to the PbS-QD particles in the composite. Composite III has the optimum crystalline behavior with the highest peaks intensities.

The chemical structures of the prepared P3MA, PbS, and P3MA/PbS-QD composites were examined by FTIR, as shown in Figure 4(d). The band positions for all P3MA, PbS, and P3MA/PbS-QD composites are summarized in Table 1. The PbS functional groups appear clearly in this figure (black line), in which the vibration of heteropolar PbS

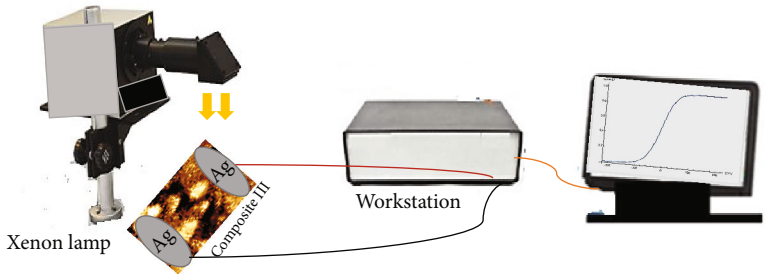

Figure 1: The schematic diagram of the electrochemical measurements for the glass/PANI/PbS photodetector using the power station under xenon lamp illumination.

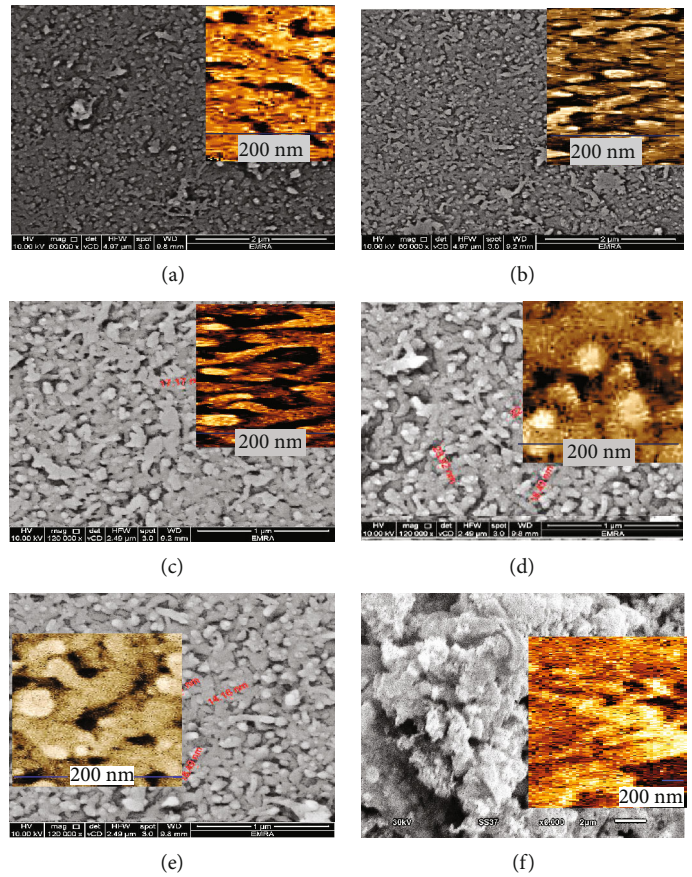

Figure 2: The SEM image of (a) P3MA, (b–e) P3MA/PbS-QD composite with different Pb^{2+} ion concentrations of 0.01, 0.03, 0.05, and 0.07 M, respectively, and (f) PbS-QD/nanoparticles.

diatomic molecules appears at 1400 and 1061 cm^{-1}. On the other hand, the stretching vibration of N-H, C-H, and C–N groups appears at 3401, 2918, and 1105 cm^{-1}, respectively, corresponding to the P3MA functional groups (red line). In contrast, the C=C benzenoid and quinoid ring bands appear at 1301 and 1467 cm^{-1}, respectively. The FTIR curves of P3MA/PbS-synthesized QD composites I, II, III, and IV with various Pb^{2+} concentrations 0.01, 0.03, 0.05, and 0.07 M, respectively, are shown in Figure 4(d). The functional groups of these composites are similar to those exhibited by both P3MA and PbS, with different shifts in band positions. After the composite formation, the N-H, C=C quinoid, and C–N vibrations shifted to average band positions 3424, 1470, and 1105 cm^{-1}, respectively. Moreover, the vibration of the C=C benzenoid ring shifted to 1291 cm^{-1}. We can conclude that composite III has the optimum band area based on these data.

The optical analyses are essential to confirm the possibility of the prepared materials to be applied as optoelectronic materials. Figure 4(e) shows the absorption spectra of the P3MA, PbS, and P3MA/PbS-QD composites I, II, III, and IV. The absorption spectrum of P3MA reveals three absorption peaks at 304, 430, and 820 nm in the UV, Vis, and NIR regions, respectively. These peaks resulted from the Π-Π^*

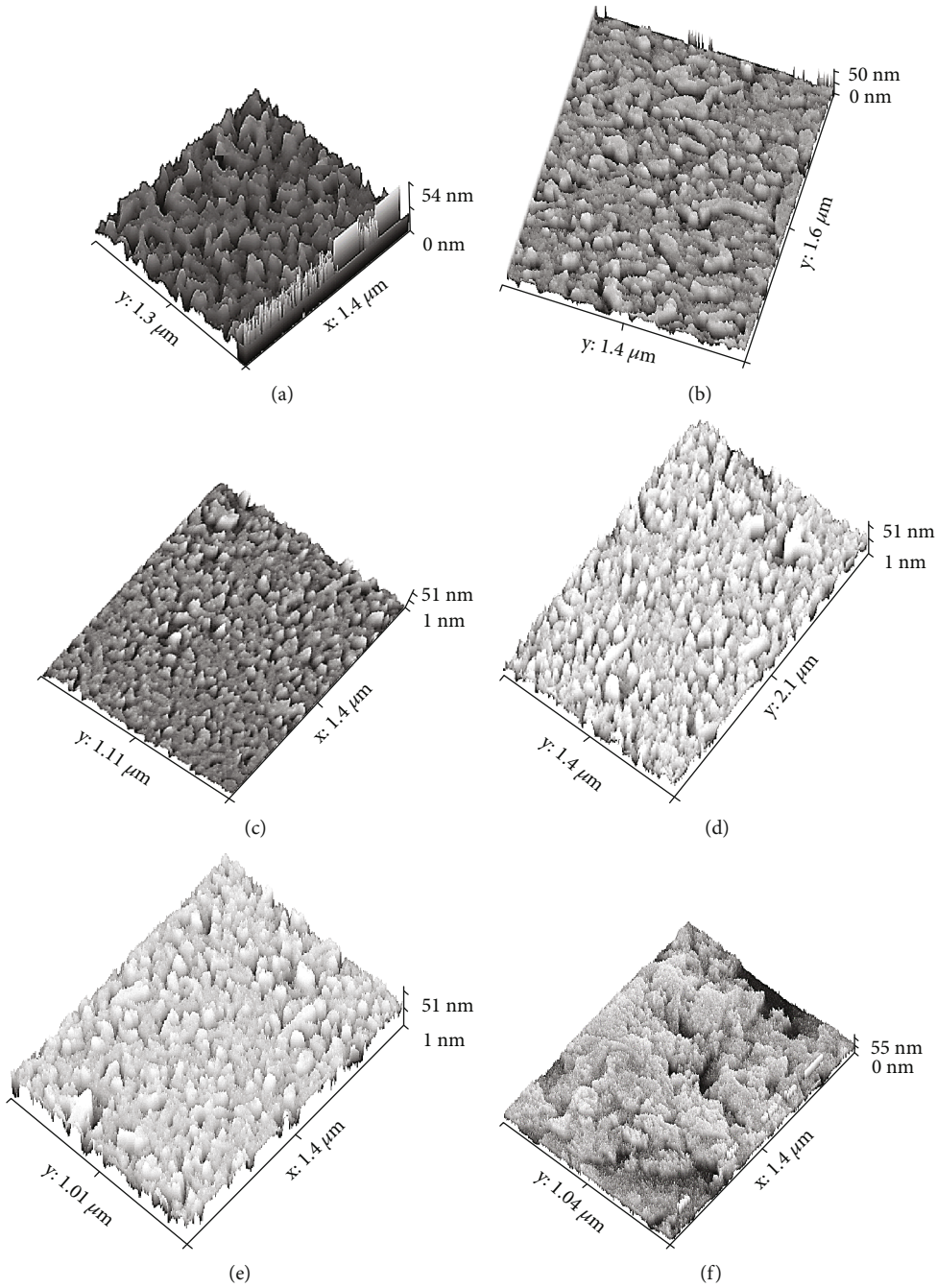

Figure 3: The cross-section and morphology of (a) P3MA, (b–e) P3MA/PbS-QD composite in different Pb^{2+} ion concentrations of 0.01, 0.03, 0.05, and 0.07 M, respectively, and (f) PbS-QD/nanoparticles.

and the conjugation of the aromatic ring [28]. Similarly, PbS has two peaks in the UV at 295 nm and Vis regions at 480 nm. These peaks resulted from the electron transfer and vibration in UV and Vis regions, respectively. The PbS dark color is the main reason for the high absorption spectra in a broad region of the absorption spectrum. It helps in the photons captured in the PbS materials and causes the electron vibration process. The P3MA/PbS-QD composites exhibit an enhanced absorption behavior that covers the UV and Vis regions, in which there is a semihump peak at 330 nm and a wide peak at 630 nm extended in a broad Vis region. The intensity of the peaks increases with increasing the Pb^{2+} concentration in the composite up to 0.05 M. Nonetheless, a decrease in the intensity was noticed at 0.07 M, which may be related to the etching PbS from the P3MA surface with a higher Pb^{2+} concentration. In conclusion, composite III has the optimum absorption behavior to be the material of choice for optoelectronic applications.

The absorption coefficient (α) was then evaluated from the absorption values (Abs) and the film thickness (d)

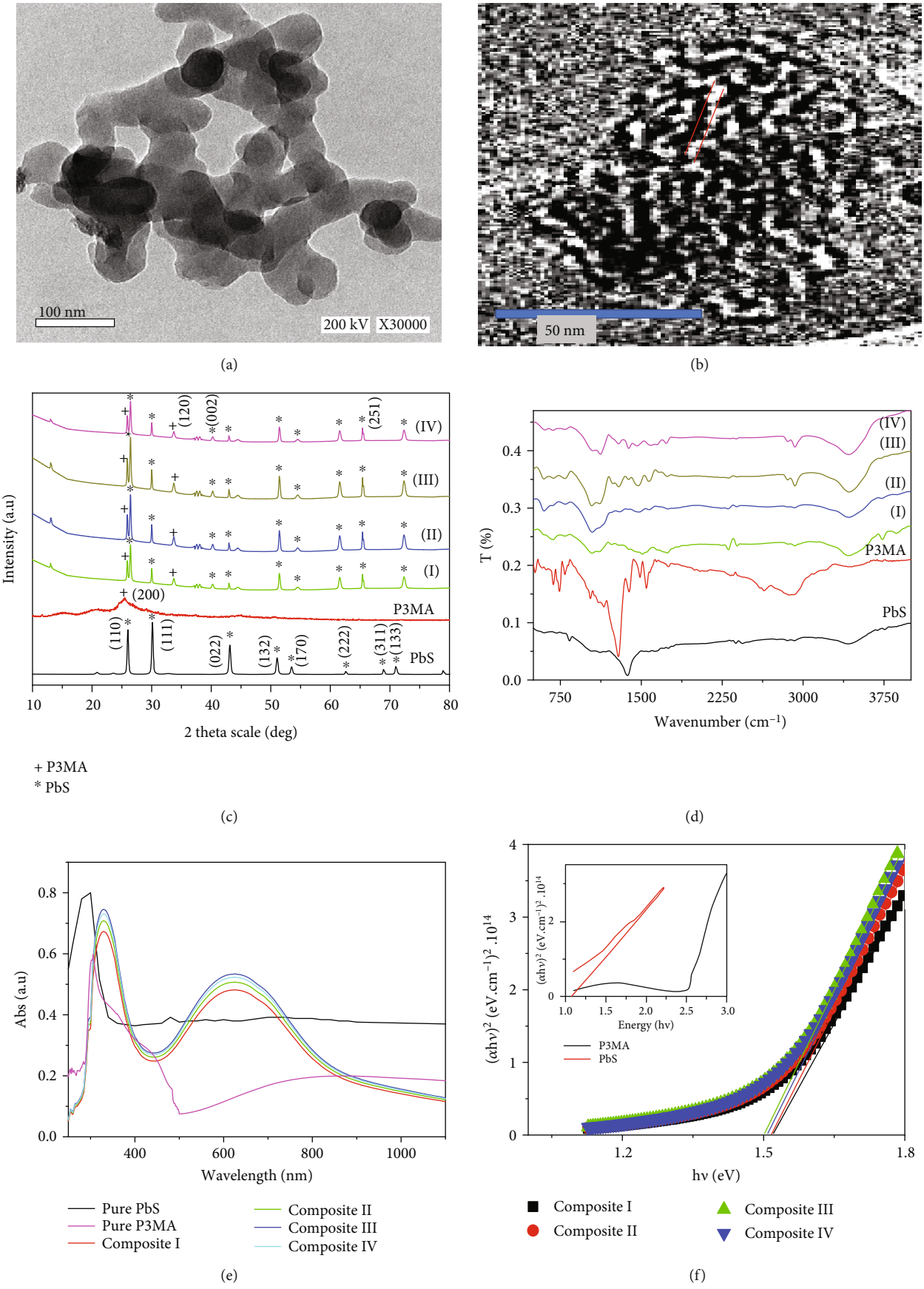

Figure 4: (a and b) TEM of composite III under different scale pares. (c) The XRD, (d) FTIR, (e) optical absorbance, and (f) band gap for P3MA, PbS, and P3MA/PbS-QD composites I, II, III, and IV under different Pb^{2+} concentrations.

utilizing the following equation [29]:

$$\alpha = \left(\frac{2.303}{d}\right)A. \quad (1)$$

The band gap of the P3MA/PbS composites was calculated through the Tauc equation below [30].

$$\alpha h\nu = A(h\nu - \mathrm{Eg})^{1/2}, \quad (2)$$

where A is a constant, h is Planck's constant, and ν is the frequency.

The band gaps for P3MA, PbS, and P3MA/PbS composites I, II, III, and IV nanomaterials are revealed in Figure 4(f) with values of 2.58, 1.1, 1.53, 1.52, 1.50, and 1.51 eV, respectively. This band gap of PbS-QD particles (1.1 eV) matches well its preparation size (5 nm), as mentioned in other studies in the literature [31–33]. Based on these values, composite III has the optimum band gap, close to the optimum band gap of 1.2 to 1.3 eV [34], which qualifies this material to be a highly efficient optoelectronic photodetector for light detection in UV, Vis, and NIR regions.

3.2. The Photodetector Electrochemical Study

3.2.1. Effect of Various Monochromatic Light. The response of the prepared photodetector, glass/P3MA/PbS (composite III), at various wavelengths from 390 to 636 nm is shown in Figure 5(a). From this figure, the produced current density in the dark (J_o) has a very low value of 0.005 mA.cm^{-2}, related to the original charges on the semiconductor P3MA/PbS-QD composite. These changes in monochromatic light can prove the responsivity of the optoelectronic to different light regions and then prove the efficiency of the device [30, 42].

Moreover, the produced J_{ph} values at bias voltage (1.0 V) are presented in Figure 5(b). Based on both figures, we notice that the photodetector responded highly to the various light wavelengths. The J_{ph} values decreased from 0.028 to 0.022 mA.cm^{-2} under multiple wavelengths from 390 to 500 nm. On the other hand, the J_{ph} values increased from 0.022 to 0.024 mA.cm^{-2}, with increasing the wavelengths from 500 to 636 nm, respectively. These variations in the J_{ph} values can be related to the disparity of the composite response to light, as previously proved in the optical analyses (Figure 4(e)). These variations in the J_{ph} values correspond to the response rate of the optoelectronic photodetector to light [28, 38, 39]. This means that the photodetector responds to a broad light region with different high sensitivities in UV and NIR regions. However, the visible region has a medium sensibility for the photodetector.

Based on the J_{ph} values obtained, the glass/P3MA/PbS photodetector has a high light response in UV and NIR and less in some visible regions. The high J_{ph} values in these blue and red sides are related to the high frequency and electron vibrations [40, 41]. To complete the electron circles after being collected on the surface, the holes are collected on the other electrode's side [29, 30, 38].

The high P3MA porosity surface and the PbS-QD particles' active sites led to the high J_{ph} value of 0.028 mA.cm^{-2}, through a minimal potential range (-1 to +1 V). So these composites' morphologies maximize the photodetector light response, especially with incorporating these QD particles' light spots of PbS.

Consequently, the prepared glass/P3MA/PbS photodetector has a high advantage in light sensing and detection in wide UV, Vis, and NIR regions. Moreover, the device has economic benefits, including the low-cost and easy preparation, that qualify the photodetector for potential industrial applications.

The effect of on/off chopped light, at very low bias voltage, on the photodetector response is shown in Figure 5(c). The photodetector has high light sensitivity under on and off chopped light. The dark current (J_d) has a small value of 0.1 μA.cm^{-2} due to charge accumulation on the electrode under applied voltage [43]. Furthermore, this value can be negligible and cannot be compared to the J_{ph} value under light irradiation. The periodic decreasing and increasing J_{ph} values yield the reproducibility of the electrode. The photodetector has excellent reproducibility with a standard deviation of 2.0%, reflecting the stability of the photodetector for light detection and sensing. The obtained results are great in comparison with polyaniline/MgZnO, in which the produced J_{ph} was 12 PA at -1.0 V [44], or with triphenylamine photodetcot that has an optimum J_{ph} value of 0.001 mA at 0 V [24].

3.2.2. Optoelectronic Device Efficiency. The glass/P3MA/PbS (composite III) photodetector responds and senses the photon flux efficiently. This can be determined by calculating both R and D values. The values of R and D can reflect the degree of responsivity of the optoelectronic device to light [45]. The R value [46] is determined referring to Equation (3), depending on light intensity (P), and both J_{ph} and J_d values, for the light and dark, respectively. Equation (3) was applied through Figure 6 under different wavelengths. This figure reveals the photodetector's response under different wavelengths from 390 to 636nm. The optimum R value is 0.29mA.W^{-1} at 390nm. The R values decrease to 0.21mA.W^{-1} and increase to 0.23mA.W^{-1} at 500 and 636nm.

$$R = \frac{J_{ph} - J_d}{P}, \quad (3)$$

$$D = R\sqrt{\frac{A}{2eJ_d}}. \quad (4)$$

The D values were calculated from Equation (4), in which R is the main function with electron charge (e), surface area (A), and dark current. D has the optimum value of 6.5×10^7 Jones at 390 nm. The D values decreased to 4.7×10^7 Jones at 500 nm and then increased to 5×10^7 Jones at 636 nm. Both R and D values confirm the photodetector responsivity to light in broad optical regions of UV, Vis, and NIR.

Table 1: A summary of the FTIR band positions for P3MA, PbS, and P3MA/PbS.

Band position (cm^{-1}) Composite (I)	(II)	(III)	(IV)	P3MA	PbS	Assignment
3424	3424	3424	3424	3401	—	N–H amino groups in P3MA [35]
2919 2860	2924 2856	2924 2856	2924 2858	2918	—	C-H aromatic ring [36]
1572	1571	1570	1590	1561	—	The coordinated water molecule [37]
1475	1470	1470	1460	1467	—	C=C quinoid ring [28]
1383	1382	1382	1384	—	1400	Heteropolar PbS diatomic molecules [38]
1293	1291	1291	1289	1301	—	C=C benzenoid rings [39]
1090	1113	1108	1121	1105	—	C–N in P3MA [40]
1045	1040	1043	1049	1049	1061	Heteropolar PbS diatomic molecules [41]
795	792	792	792	789	—	C–H in-plane [29]
599	597	590	608	587	—	Para disubstituted aromatic rings

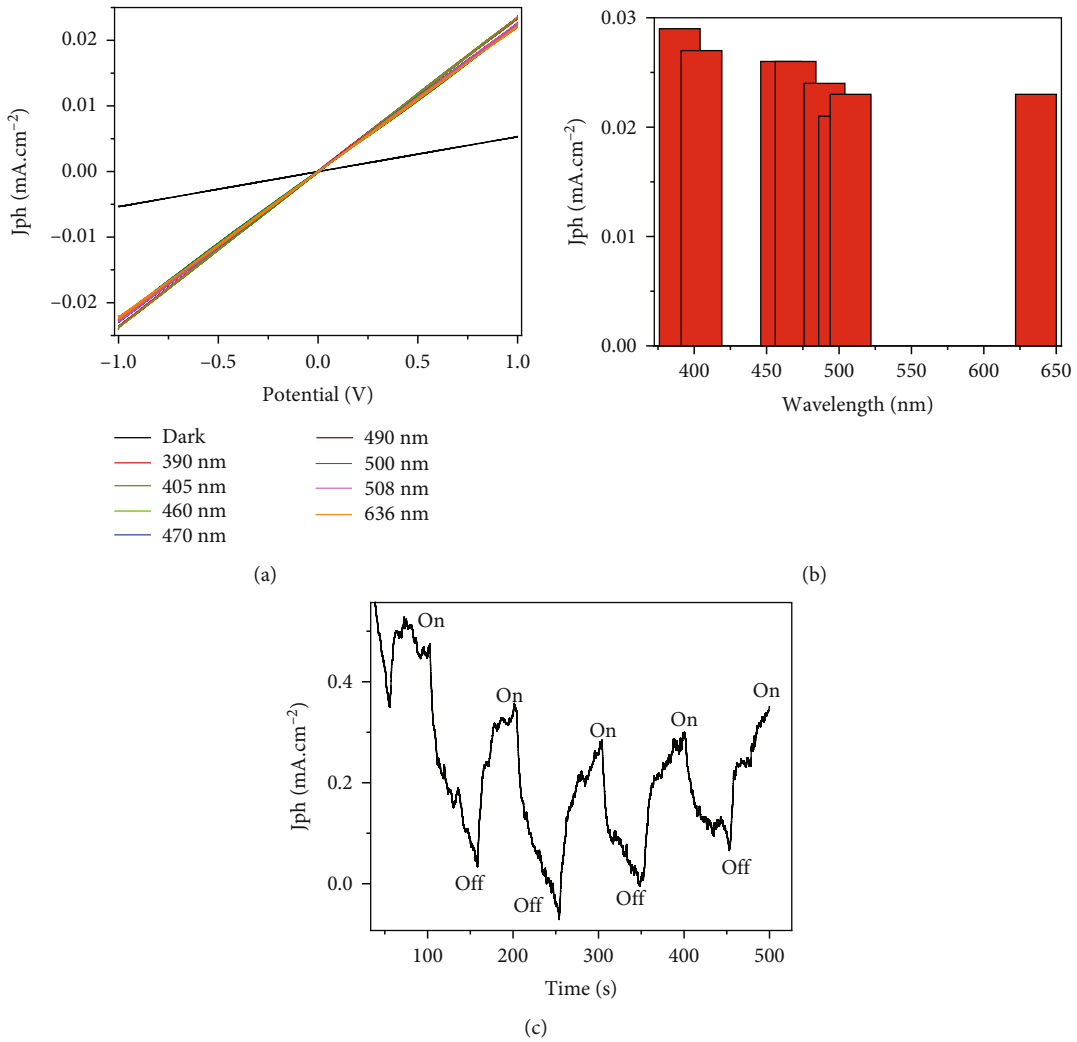

Figure 5: (a) The influence of dark and light wavelengths, (b) current density at 1.0 V, and (c) on/off chopped current for glass/P3MA/PbS photodetector at 25°C.

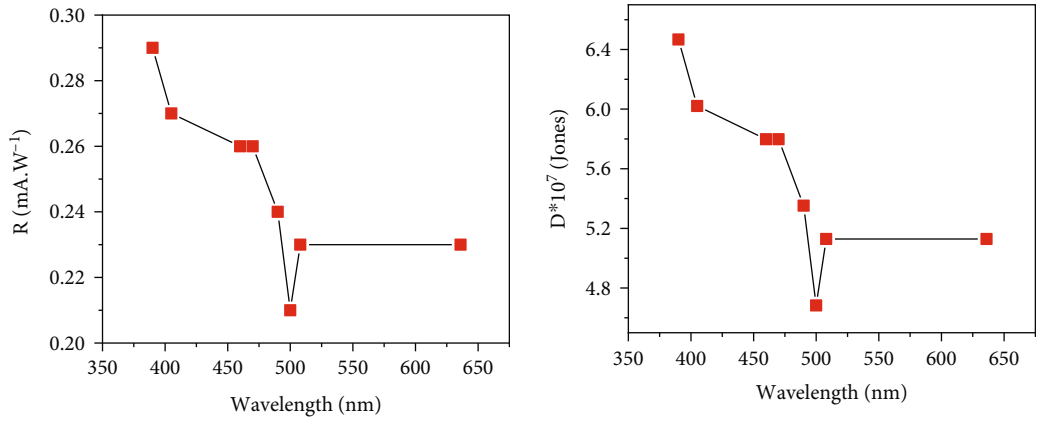

Figure 6: (a) R and (b) D values of the glass/P3MA/PbS photodetector.

Table 2: Comparison of the photoresponsivity of the synthesized glass/P3MA/PbS photodetector with previous works.

Structure [reference]	Wavelength (nm)	Bias (V)	R (mA.W^{-1})
Polyaniline/MgZnO [44]	250	5	0.1
Graphene/P3HT [47]	325	1	NA
2,1,3-Benzothiadiazole [23]	734	0	NA
Polyvinylpyrrolidone/ $CsPbBr_3$ [22]	500	2	NA
Triphenylamine [24]	360	0	NA
GO/Cu_2O [48]	300	2	0.5
CuO nanowires [11]	390	5	—
TiN/TiO_2 [15]	550	5	—
TiO_2/NiO [49]	350	0	0.25
Al-CdS [50]	532	5	0.1
CdS-ZnO [14]	460	1	—
TiN/TiO_2 [15]	550	5	—
GO/Cu_2O [48]	300	2	0.28
Glass/P3MA/PbS-QD (this work)	390	1	0.29

This broad light response is related to a large number of active sites in P3MA/PbS-QD particles. The PbS particles represent the light spots that can detect and capture the light photons that cause electron resonance. This process transfers additional electrons from the P3MA to its surface to generate the J_{ph} values, transferring the hole in the opposite direction.

The electron transfer sequence is the photodetector's operation in the abroad light region. This unique property makes the synthesized optoelectronic photodetector overcome the drawbacks of the previous literature studies (mentioned in the introduction section).

In addition, Table 2 includes a comparison of the R values obtained in this study to those obtained in the previous literature studies. Based on these results, we can conclude a bright possible future for this optoelectronic photodetector for industrial applications with high financial returns.

3.3. The Plausible Mechanism of the Light Sensing. The light sensing mechanism of the glass/P3MA/PbS optoelectronic device depends on the band energy theory (Figure 7(a)). The schematic structure of the composite is mentioned in Figure 7(b). The electrons liberated under the photon flux have two motions hole-electron transfer (charge transfer). This transfer is only related to the hot electrons passing from the valency band to the conducting band. The second process is the accumulations of the electrons on the lowest conducting band level material. Under the two processes of electron transfer and accumulation, the local electromagnetic field is established around the semiconductor materials in which the produced electrons can effectively produce J_{ph} [52–60]. The PbS-QD is inserted between the P3MA chains; these facilitate the electron transfer and its accumulation on PbS surface.

There is a great advantage for the P3MA/PbS composite, in which the band gap is 1.50 eV with a minimal depletion layer, and the electrons can be easily transferred from the P3MA to PbS. This electron transfer reflects the high value of 0.029 mA.cm^{-2} (Figure 5(a)). The absence of the depletion layer causes the continuous flow of free electrons from P3MA to PbS-QD particles [51]. The large surface area of PbS materials enhances the acceptance of electrons from P3MA material, in which all the active sites are ready for acceptance the electrons from P3MA. Therefore, the prepared optoelectronic device can be applied for light sensing and detecting in abroad light regions: UV, Vis, and NIR.

4. Conclusions

A novel polymer-based optoelectronic photodetector glass/P3MA/PbS was synthesized and assessed for light sensing and detection in UV, Vis, and NIR regions. This photodetector has R and D values having optimum values of 0.29 mA.W^{-1} and 6.5×10^7 Jones, respectively, at 390 nm. The great advantage was represented in the high efficiency

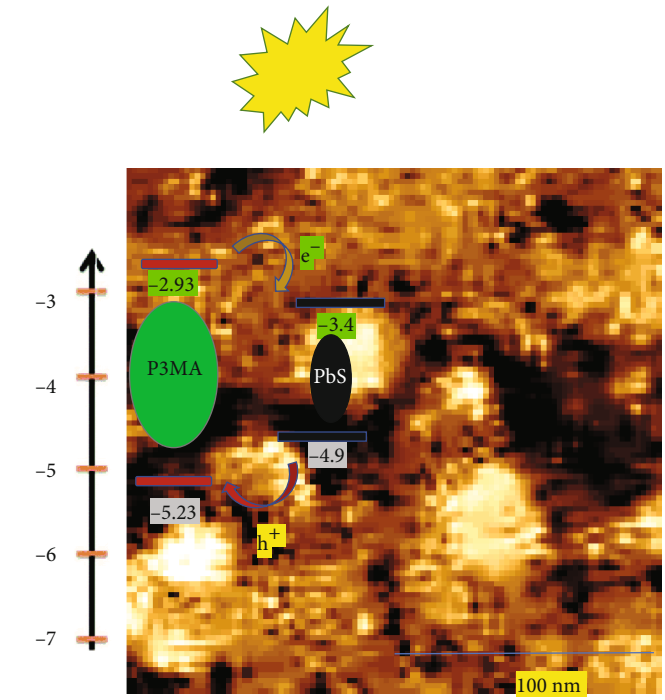

Figure 7: (a) The plausible mechanism of the glass/P3MA/PbS optoelectronic photodetector device and (b) the schematic diagram of the composite structure.

and the low preparation costs, in which the photodetector device of $10 \times 10\,cm^2$ area costs less than 1.0 $. Soon our team works on a prototype for an industrial application. This trend is based on the highly optoelectronic properties of these materials, with its low cost and easy preparation process. This optoelectronic device will be a great part of highly technology devices such as camera and spacecrafts.

Data Availability

All the data are mentioned in the manuscript, and there is no supporting data.

Conflicts of Interest

The authors declare no conflict of interest.

Acknowledgments

This research was funded by the Deanship of Scientific Research at Jouf University, grant number DSR-2021-03-0320.

References

[1] F. Zhong, H. Wang, Z. Wang et al., "Recent progress and challenges on two-dimensional material photodetectors from the

perspective of advanced characterization technologies," *Nano Research*, vol. 14, no. 6, pp. 1840–1862, 2021.

[2] C. Liu, J. Guo, L. Yu et al., "Silicon/2D-material photodetectors: from near-infrared to mid-infrared," *Light: Science & Applications*, vol. 10, no. 1, p. 123, 2021.

[3] R. Maiti, C. Patil, M. A. S. R. Saadi et al., "Strain-engineered high-responsivity MoTe2 photodetector for silicon photonic integrated circuits," *Nature Photonics*, vol. 14, no. 9, pp. 578–584, 2020.

[4] A. M. Elsayed, M. Shaban, A. H. Aly, A. M. Ahmed, and M. Rabia, "Preparation and characterization of a high-efficiency photoelectric detector composed of hexagonal Al2O3/TiO2/TiN/Au nanoporous array," *Materials Science in Semiconductor Processing*, vol. 139, p. 106348, 2022.

[5] A. M. Elsayed, M. Rabia, M. Shaban, A. H. Aly, and A. M. Ahmed, "Preparation of hexagonal nanoporous Al2O3/TiO2/TiN as a novel photodetector with high efficiency," *Scientific Reports*, vol. 11, pp. 1–12, 2021.

[6] N. Flöry, P. Ma, Y. Salamin et al., "Waveguide-integrated van Der Waals heterostructure photodetector at telecom wavelengths with high speed and high responsivity," *Nature Nanotechnology*, vol. 15, no. 2, pp. 118–124, 2020.

[7] P. Fan, U. K. Chettiar, L. Cao, F. Afshinmanesh, N. Engheta, and M. L. Brongersma, "An invisible metal–semiconductor photodetector," *Nature Photonics*, vol. 6, no. 6, pp. 380–385, 2012.

[8] M. Rabia, S. H. Mohamed, H. Zhao, M. Shaban, Y. Lei, and A. M. Ahmed, "TiO2/TiOxNY hollow mushrooms-like nanocomposite photoanode for hydrogen electrogeneration," *Journal of Porous Materials*, vol. 27, no. 1, pp. 133–139, 2020.

[9] A. Almohammedi, M. Shaban, H. Mostafa, and M. Rabia, "Nanoporous TiN/TiO2/alumina membrane for photoelectrochemical hydrogen production from sewage water," *Nanomaterials*, vol. 11, no. 10, article 2617, 2021.

[10] A. A. A. Abdelazeez, N. M. A. Hadia, M. Alzaid et al., "Development of CuO nanoporous material as a highly efficient optoelectronic device," *Applied Physics A*, vol. 128, p. 321, 2022.

[11] S. B. Wang, C. H. Hsiao, S. J. Chang et al., "A CuO nanowire infrared photodetector," *Sensors and Actuators A: Physical*, vol. 171, no. 2, pp. 207–211, 2011.

[12] Z. Bai and Y. Zhang, "Self-powered UV-visible photodetectors based on ZnO/Cu_2O nanowire/electrolyte heterojunctions," *Journal of Alloys and Compounds*, vol. 675, pp. 325–330, 2016.

[13] Q. Hong, Y. Cao, J. Xu, H. Lu, J. He, and J. L. Sun, "Self-powered ultrafast broadband photodetector based on p-n heterojunctions of CuO/Si nanowire array," *ACS Applied Materials & Interfaces*, vol. 6, no. 23, pp. 20887–20894, 2014.

[14] M. Shuai, Y. Lingmin, C. Lei, L. Chun, Y. Mingli, and F. Xinhui, "Resistive-type UV-visible photodetector based on CdS NWs /ZnO nanowalls heterostructure fabricated using in-situ synthesis method," *Journal of Alloys and Compounds*, vol. 827, p. 154090, 2020.

[15] A. Naldoni, U. Guler, Z. Wang et al., "Broadband hot-electron collection for solar water splitting with plasmonic titanium nitride," *Advanced Optical Materials*, vol. 5, no. 15, article 1601031, 2017.

[16] M. Shaban, M. R. Abukhadra, M. Rabia, Y. A. Elkader, and M. R. Abd El-Halim, "Investigation the adsorption properties of graphene oxide and polyaniline nano/micro structures for efficient removal of toxic Cr(VI) contaminants from aqueous solutions; kinetic and equilibrium studies," *Rendiconti Lincei. Scienze Fisiche e Naturali*, vol. 29, no. 1, pp. 141–154, 2018.

[17] M. R. Abukhadra, M. Rabia, M. Shaban, and F. Verpoort, "Heulandite/polyaniline hybrid composite for efficient removal of acidic dye from water; kinetic, equilibrium studies and statistical optimization," *Advanced Powder Technology*, vol. 29, no. 10, pp. 2501–2511, 2018.

[18] M. Shaban, M. Rabia, A. M. A. El-Sayed, A. Ahmed, and S. Sayed, "Photocatalytic properties of PbS/graphene oxide/polyaniline electrode for hydrogen generation," *Scientific Reports*, vol. 7, pp. 1–13, 2017.

[19] M. Rabia, H. S. H. Mohamed, M. Shaban, and S. Taha, "Preparation of polyaniline/PbS core-shell nano/microcomposite and its application for photocatalytic H2 electrogeneration from H2O," *Scientific Reports*, vol. 8, pp. 1–11, 2018.

[20] B. Yuan, M. R. F. Aziz, S. Li, J. Wu, D. Li, and R. K. Li, "An electro-spun tri-component polymer biomaterial with optoelectronic properties for neuronal differentiation," *Acta Biomaterialia*, vol. 139, pp. 82–90, 2022.

[21] T. H. AlAbdulaal and I. S. Yahia, "Analysis of optical linearity and nonlinearity of Fe3+- doped PMMA/FTO polymeric films: new trend for optoelectronic polymeric devices," *Physica B: Condensed Matter*, vol. 601, p. 412628, 2021.

[22] A. V. Fulari, N. T. Duong, D. A. Nguyen et al., "Achieving direct electrophoretically deposited highly stable polymer induced CsPbBr3 colloidal nanocrystal films for high-performance optoelectronics," *Chemical Engineering Journal*, vol. 433, article 133809, 2022.

[23] Y. Liu, P. Guo, P. Gao et al., "Effect of fluorine atoms on optoelectronic, aggregation and dielectric constants of 2,1,3-benzothiadiazole-based alternating conjugated polymers," *Dyes and Pigments*, vol. 193, p. 109486, 2021.

[24] H. J. Yen and G. S. Liou, "Design and preparation of triphenylamine-based polymeric materials towards emergent optoelectronic applications," *Progress in Polymer Science*, vol. 89, pp. 250–287, 2019.

[25] S. Zheng, J. Chen, E. M. J. Johansson, and X. Zhang, "PbS colloidal quantum dot inks for infrared solar cells," *iScience*, vol. 23, no. 11, article 101753, 2020.

[26] B. Sun, A. Johnston, C. Xu et al., "Monolayer perovskite bridges enable strong quantum dot coupling for efficient solar cells," *Joule*, vol. 4, no. 7, pp. 1542–1556, 2020.

[27] S. Chan, M. Liu, K. Latham et al., "Monodisperse and size-tunable PbS colloidal quantum dots via heterogeneous precursors," *Journal of Materials Chemistry C*, vol. 5, no. 8, pp. 2182–2187, 2017.

[28] S. M. Sayyah, M. Shaban, and M. Rabia, "Electropolymerization of m-toluidin on platinum electrode from aqueous acidic solution and character of the obtained polymer," *Advances in Polymer Technology*, vol. 37, 136 pages, 2018.

[29] E.-S. M. Sayyah, M. Shaban, and M. Rabia, "A sensor of m-cresol nanopolymer/Pt-electrode film for detection of lead ions by potentiometric methods," *Advances in Polymer Technology*, vol. 37, 1304 pages, 2018.

[30] J. Y. Kim, V. Adinolfi, B. R. Sutherland et al., "Single-step fabrication of quantum funnels via centrifugal colloidal casting of nanoparticle films," *Nature communications*, vol. 6, pp. 1–9, 2015.

[31] S. Kaci, A. Keffous, L. Guerbous, and M. Trari, "Preparation and room temperature photoluminescence characterization

of PbS/Si(100) thin films," *Thin Solid Films*, vol. 520, no. 1, pp. 79–82, 2011.

[32] M. Liu, Q. Zhan, W. Li, R. Li, Q. He, and Y. Wang, "Effect of Zn doping concentration on optical band gap of PbS thin films," *Journal of Alloys and Compounds*, vol. 792, pp. 1000–1007, 2019.

[33] A. K. Bhunia, T. Kamilya, and S. Saha, "Photo relaxation change and emission quenching in different sizes of PbS-nanoparticles-protein corona," *Chemistry Select*, vol. 1, no. 18, pp. 5768–5778, 2016.

[34] S. Laalioui, K. B. Alaoui, H. A. Dads, K. AssaliEl, B. Ikken, and A. Outzourhit, "Progress in perovskite based solar cells: scientific and engineering state of the art," *Reviews on Advanced Materials Science*, vol. 59, no. 1, pp. 10–25, 2020.

[35] S. M. Sayyah, M. Shaban, and M. Rabia, "A sensor of M-toluidine/m-cresol polymer film for detection of lead ions by potentiometric methods," *Sensor Letters*, vol. 14, no. 5, pp. 522–529, 2016.

[36] S. M. Sayyah, M. Shaban, and M. Rabia, "M-toluidine polymer film coated platinum electrode as a PH sensor by potentiometric methods," *Sensor Letters*, vol. 13, no. 11, pp. 961–966, 2015.

[37] N. M. A. Hadia, M. A. H. Khalafalla, F. M. Abdel Salam et al., "Conversion of sewage water into H_2 gas fuel using hexagonal nanosheets of the polyaniline-assisted deposition of PbI_2 as a nanocomposite photocathode with the theoretical qualitative ab-initio calculation of the H_2O splitting," *Polymers*, vol. 14, no. 11, p. 2148, 2022.

[38] N. M. A. Hadia, A. A. A. Abdelazeez, M. Alzaid et al., "Converting Sewage Water into H_2 Fuel Gas Using Cu/CuO Nanoporous Photocatalytic Electrodes," *Materials*, vol. 15, no. 4, p. 1489, 2022.

[39] S. M. Sayyah, M. Shaban, and M. Rabia, "A high-sensitivity potentiometric mercuric ion sensor based on m-toluidine films," *IEEE Sensors Journal*, vol. 16, no. 6, pp. 1541–1548, 2016.

[40] M. Rabia, N. M. A. Hadia, O. M. Farid, A. A. A. Abdelazeez, S. H. Mohamed, and M. Shaban, "Poly(m-toluidine)/rolled graphene oxide nanocomposite photocathode for hydrogen generation from wastewater," *International Journal of Energy Research*, vol. 46, no. 9, pp. 11943–11956, 2022.

[41] M. A. Awad, M. Shaban, and M. Rabia, "The efficiency of M (M = Li, Na, or Cs) doped CdS nanomaterials in optoelectronic applications," *International Journal of Energy Research*, vol. 46, no. 6, pp. 8443–8451, 2022.

[42] Y. Lei, Y. Chen, R. Zhang et al., "A fabrication process for flexible single-crystal perovskite devices," *Nature*, vol. 583, pp. 790–795, 2020.

[43] A. A. A. Abdelazeez, N. M. A. Hadia, A. H. I. Mourad et al., "Effect of Au Plasmonic Material on Poly M-Toluidine for Photoelectrochemical Hydrogen Generation from Sewage Water," *Polymers*, vol. 14, no. 4, p. 768, 2022.

[44] H. Chen, P. Yu, Z. Zhang et al., "Ultrasensitive self-powered solar-blind deep-ultraviolet photodetector based on all-solid-state polyaniline/MgZnO bilayer," *Small*, vol. 12, no. 42, pp. 5809–5816, 2016.

[45] H. Park, J. Lee, G. Han et al., "Nano-patterning on multilayer MoS2 via block copolymer lithography for highly sensitive and responsive phototransistors," *Communications Materials*, vol. 2, pp. 1–9, 2021.

[46] R. Jia, D. Zhao, N. Gao, and D. Liu, "Polarization enhanced charge transfer: dual-band GaN-based plasmonic photodetector," *Scientific Reports*, vol. 7, pp. 1–8, 2017.

[47] W. C. Tan, W. H. Shih, and Y. F. Chen, "A highly sensitive graphene-organic hybrid photodetector with a piezoelectric substrate," *Advanced Functional Materials*, vol. 24, no. 43, pp. 6818–6825, 2014.

[48] T. Lan, A. Fallatah, E. Suiter, and S. Padalkar, "Size controlled copper (I) oxide nanoparticles influence sensitivity of glucose biosensor," *Sensors*, vol. 17, no. 9, 2017.

[49] L. Zheng, F. Teng, Z. Zhang, B. Zhao, and X. Fang, "Large scale, highly efficient and self-powered UV photodetectors enabled by all-solid-state n-TiO2 nanowell/p-NiO mesoporous nanosheet heterojunctions," *Journal of Materials Chemistry C*, vol. 4, no. 42, pp. 10032–10039, 2016.

[50] K. D. A. Kumar, P. Mele, S. Golovynskyi et al., "Insight into Al doping effect on photodetector performance of CdS and CdS:Mg films prepared by self-controlled nebulizer spray technique," *Journal of Alloys and Compounds*, vol. 892, article 160801, 2022.

[51] S. Podder and A. R. Pal, "Plasmonic visible-NIR photodetector based on hot electrons extracted from nanostructured titanium nitride," *Journal of Applied Physics*, vol. 126, no. 8, article 083108, 2019.

[52] F. Mohamed, M. Rabia, and M. Shaban, "Synthesis and characterization of biogenic iron oxides of different nanomorphologies from pomegranate peels for efficient solar hydrogen production," *Journal of Materials Research and Technology*, vol. 9, no. 3, pp. 4255–4271, 2020.

[53] M. Rabia, M. Shaban, A. Adel, and A. A. Abdel-Khaliek, "Effect of plasmonic Au nanoparticles on the photoactivity of polyaniline/indium tin oxide electrodes for water splitting," *Environmental Progress & Sustainable Energy*, vol. 38, no. 5, p. 13171, 2019.

[54] M. Rabia, M. Shaban, B. M. Jibali, and A. A. Abdelkhaliek, "Effect of annealing temperature on the photoactivity of ITO/VO 2 (M)/Au film electrodes for water splitting," *Journal of Nanoscience and Nanotechnology*, vol. 20, no. 7, pp. 4120–4130, 2020.

[55] Z. Liu, F. Li, S. Li et al., "Fabrication of UV photodetector on TiO_2/diamond film," *Scientific Reports*, vol. 5, no. 1, article 14420, 2015.

[56] M. Shaban, M. Benghanem, A. Almohammedi, and M. Rabia, "Optimization of the active layer P3HT:PCBM for organic solar cell," *Coatings*, vol. 11, no. 7, p. 863, 2021.

[57] M. Shaban, M. Rabia, M. G. Eldakrory, R. M. Maree, and A. M. Ahmed, "Efficient photoselectrochemical hydrogen production utilizing of <scp> APbI $_3$ </Scp> (A = Na, Cs, and Li) perovskites nanorods," *International Journal of Energy Research*, vol. 45, no. 5, pp. 7436–7446, 2021.

[58] A. Helmy, M. Rabia, M. Shaban, A. M. Ashraf, S. Ahmed, and A. M. Ahmed, "Graphite/rolled graphene oxide/carbon nanotube photoelectrode for water splitting of exhaust car solution," *International Journal of Energy Research*, vol. 44, no. 9, pp. 7687–7697, 2020.

[59] A. A. Hussain, B. Sharma, T. Barman, and A. R. Pal, "Self-powered broadband photodetector using plasmonic titanium nitride," *ACS Applied Materials & Interfaces*, vol. 8, no. 6, pp. 4258–4265, 2016.

[60] A. A. Hussain, A. R. Pal, and D. S. Patil, "An efficient fast response and high-gain solar-blind flexible ultraviolet photodetector employing hybrid geometry," *Applied Physics Letters*, vol. 104, no. 19, p. 193301, 2014.